Bulletin of the Seismological Society of America, Vol. 105, No. 4, pp. 1931–1946, August 2015, doi: 10.1785/0120140327

Ⓔ

Rupture and Ground-Motion Models on the Northern San Jacinto Fault, Incorporating Realistic Complexity

by Julian C. Lozos,* David D. Oglesby, James N. Brune, and Kim B. Olsen

Abstract We use the 3D finite-element method to conduct dynamic models of rupture and resulting ground motion on the Claremont–Casa Loma stepover of the northern San Jacinto fault. We incorporate complex fault geometry (from the U.S. Geological Survey [USGS] Quaternary Faults Database; see Data and Resources), a realistic velocity structure (the Southern California Earthquake Center Community Velocity Model-S), a realistic regional stress field with an orientation taken from seismicity relocation literature, and several stochastic self-similar shear stress distributions. As we incorporate more types of complexity, the specific effects of any individual factor become less apparent within the overall rupture behavior. We also find that the distribution of high and low shear stress that arises from combining regional and stochastic stress fields has the strongest control over where the rupture terminates. Using a regional stress field alone, as well as with the combined regional and stochastic stress realization, we find that the stepover presents a significant barrier to rupture, regardless of our choice of initial nucleation point and that it is difficult for rupture to propagate the full length of either fault segment. Greater heterogeneity of stresses tends to produce shorter ruptures. Within this result, we find that the Claremont strand is more favorable for long ruptures than the Casa Loma–Clark strand. Low-frequency ground-motion intensity and distribution are controlled largely by the velocity structure rather than by stress heterogeneity. The strongest motions produced in these models are in the San Bernardino basin. Although directivity effects do contribute to the low-frequency ground-motion distribution, particularly in the near field, they are secondary to the effects of the velocity structure.

Online Material: Figures of ground motions from models used to calibrate the stress conditions for dynamic rupture propagation.

Introduction

The San Jacinto fault (SJF) is a 230-km-long right-lateral strike-slip fault that is one of the major components of the plate boundary in southern California (Fig. 1). It branches off from the San Andreas fault in Cajon Pass and runs subparallel to it through to the Imperial Valley. The SJF is a young fault, which has not yet matured into a single primary strand; it is characterized by geometrical complexity. Strand boundaries within the SJF are generally delineated by bends, branches, and stepovers, but the complexity within each strand is such that several different parameterizations exist for the fault zone as a whole (Wesnousky, 1986; Working Group on California Earthquake Probabilities, 1995; Sanders and Magistrale, 1997; Marliyani *et al.*, 2013; U.S. Geological Survey Quaternary Faults Database, see Data and Resources).

The first major complexity along strike from the SJF's endpoint in Cajon Pass is the extensional stepover between the Claremont strand to the northeast and the Casa Loma strand to the southwest (Fig. 2). The two strands overlap each other for ~25 km along strike and are separated by a distance of 2.5–5 km over that length. Both strands include substantial geometrical complexity within their surface traces, in the form of smaller bends and discontinuities. One such discontinuity is a short compressional bend connecting the Casa Loma strand to the Clark strand near Hemet. A shorter intermediate fault strand, known as the Farm Road strand, is positioned at the northern end of the stepover (Park *et al.*, 1995). It is separated from the Claremont by 2 km and the Casa Loma by 1 km and may be as short as 2.4 km (U.S. Geological Survey [USGS] Quaternary Faults Database; see Data and Resources) or as long as 7 km (Marliyani *et al.*, 2013). The dip of all three segments is poorly constrained. Seismic reflection studies suggest that the Claremont and Farm Road strands, and possibly also

*Now at Department of Geophysics, Stanford University, Mitchell Building 3rd Floor, 397 Panama Mall, Stanford, California 94305.

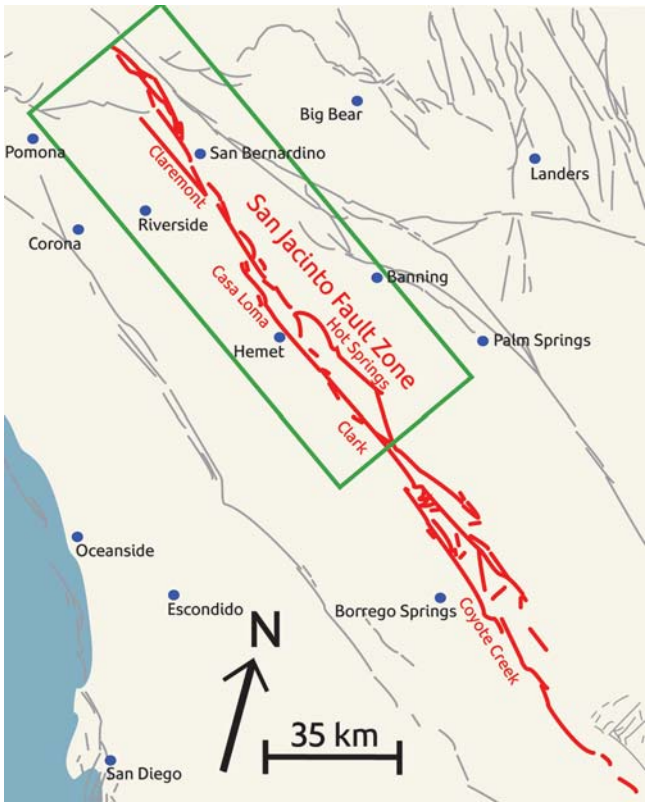

Figure 1. The location of the San Jacinto fault (SJF; red) in southern California. The part of the fault zone examined in this study is within the green box. Other Quaternary faults are shown in gray.

Figure 2. Close up of the northern SJF zone with geometry based on the U.S. Geological Survey (USGS) Quaternary Faults Database (see Data and Resources). The Claremont–Casa Loma stepover is circled in green. The Claremont strand is the more northeasterly of the two; the Casa Loma is to the southwest. The small fault within the northern end of the stepover is the Farm Road strand.

the Casa Loma–Clark, may converge to a flower structure at depth (Park *et al.*, 1995), but seismicity data suggests that the dips may be close to vertical (Lin *et al.*, 2007). A geologic study by Kendrick and Morton (2012) also suggests that, because the total offset on the SJF (~24 km) is equivalent to the overlap length of the Claremont–Casa Loma stepover, the stepover may represent an offset of distinctly separate vertical faults. The Claremont and Casa Loma strands define the edges of the San Jacinto Valley, which is a pull-apart basin with a depth of up to 2.3 km (Park *et al.*, 1995).

The Claremont–Casa Loma stepover poses several key questions about the ability of earthquake rupture to negotiate fault zone complexity. The primary question is whether or not a rupture that initiates on the Claremont strand will be able to jump onto the Casa Loma–Clark strand or vice versa. Within this issue are the questions of how the smaller-scale complexities within those strands may affect rupture propagation and whether the Farm Road strand is large enough or in an optimal position to sustain its own rupture or to affect propagation on the larger fault strands. Regardless of the extent of the rupture, the questions also arise of how complex fault geometry affects ground motion and of whether or not that effect is stronger than the effect of the complex velocity structure surrounding the fault. These physical questions also tie directly into questions of seismic hazard in this area, because the northern SJF runs through several cities, including San Bernardino, Moreno Valley, San Jacinto, and Hemet. Even a moderate rupture on the SJF would have potential to cause considerable damage throughout the densely populated Inland Empire region.

Historic earthquakes and paleoseismic evidence alike suggest there are rupture barriers in the region of the Claremont–Casa Loma stepover. In 1899 and 1918, two M_w 6+ events occurred on the northern SJF. There have been as many different assessments of the locations of these two earthquakes as there have been studies on the northern SJF. Recent paleoseismology and lidar places the 1918 event on the Clark strand, just south of the stepover region (Salisbury *et al.*, 2012; Rockwell *et al.*, 2015), whereas the location of the smaller 1899 event is still more questionable. Regardless of the exact endpoints of these ruptures, it is evident that the SJF in the vicinity of the Claremont–Casa Loma stepover can fail in a series of smaller events. Paleoseismic studies on either side of the stepover also indicate that the Claremont and Casa Loma–Clark strands alike have ruptured in multiple M_w 7+ events (Onderdonk *et al.*, 2015; Rockwell *et al.*, 2015), though the temporal resolution of these data is not precise enough to determine whether these large events involved each strand individually or both at once. Dynamic rupture modeling can help assess (1) whether the barriers that lead to this apparent segmentation are geometrical or are a result of a regional or local stress field and (2) whether a through-going rupture across the stepover is possible.

There is a large and growing body of work in which dynamic rupture models have been used to investigate the effect of a specific type of geometrical complexity on rupture propagation, including disconnected stepovers between parallel faults (Harris *et al.*, 1991; Harris and Day, 1993; Aochi *et al.*, 2000; Oglesby, 2008; Lozos *et al.*, 2012), parallel faults with another fault linking them at some angle (Magistrale and Day, 1999; Oglesby, 2005; Lozos *et al.*, 2011), and fault branches (Kame *et al.*, 2003; Duan and Oglesby, 2007). Many of these have results that are directly pertinent to the case of the northern SJF. The study of Harris and Day (1993) on the ability of rupture to jump different stepover widths found that rupture is not likely to jump across an extensional stepover with a separation wider than 4 km, which is narrower than the widest separation between the Claremont and Casa Loma strands. The studies of Lozos *et al.* (2012) and Lozos, Oglesby, *et al.* (2015) included an intermediate fault within a stepover, like the Farm Road strand between the Claremont and Casa Loma, and found that the length of the intermediate segment can have a controlling effect on whether or not rupture can jump the larger stepover. However, these studies and the others cited above use fault geometries that are planar, aside from the single discontinuity of the type for which the effect is being investigated. This type of simplification is crucial to understand primary fault physics, but it may not be adequate to describe the rupture behavior of a realistically complex fault zone.

In the present study, we investigate the ability of rupture to propagate through the Claremont–Casa Loma stepover of the northern SJF, and the ground motion that results from any ruptures in this area, by constructing dynamic rupture models that incorporate more levels of realistic complexity than in past modeling studies. In particular, we incorporate geometrical complexity within the individual strands of the larger stepover, a regional stress field taken from seismicity studies, and several randomly generated stochastic stress distributions, and we embed the fault system in an observationally determined velocity structure for southern California.

Methods

Computational Method

Our dynamic rupture models were conducted using FaultMod (Barall, 2009), a 3D finite-element code that has been rigorously tested as part of the Southern California Earthquake Center (SCEC) dynamic rupture code validation workshop (Harris *et al.*, 2009). We use a slip-weakening Coulomb friction criterion (Ida, 1972; Palmer and Rice, 1973; Andrews, 1976), and a fully elastic lossless medium. The physical and computational parameters common between all of our models are listed in Table 1; however, there is much variability between models, both due to the heterogeneity of initial stress conditions and velocity structure and to our choice of stress states. In all cases, we force initial nucleation by raising shear stress on the fault above the yield stress and forcing rupture propagation over a radius larger than the critical patch size required for self-sustaining rupture. Any secondary nucleations on other fault strands occur naturally as a result of the physics of the rupture.

Table 1
Physical and Computational Parameters

P-wave velocity	SCEC Community Velocity Model; minimum clipped to 4157 m/s
S-wave velocity	SCEC Community Velocity Model; minimum clipped to 2400 m/s
Density	SCEC Community Velocity Model
μ_{static}	0.6; variable in models with stochastic stresses
$\mu_{dynamic}$	0.2
D_0	0.4 m
Principal stresses	Variable (see Table 2)
Stress orientation	N7°E
Element size	200 m in the near field, 400 m in the far field
Nucleation radius	3000 m

μ_{static} and $\mu_{dynamic}$ are the static and dynamic coefficients of friction, respectively. D_0 is the critical slip-weakening distance. SCEC, Southern California Earthquake Center.

Ground motion is a direct output of FaultMod calculations. However, computational constraints do not allow us to use a small enough mesh size to resolve the high-frequency ground motions that pose a hazard to infrastructure. Thus, we apply a filter to our results such that only frequencies of 1 Hz or less are represented in the ground-motion plots in this study. These plots are intended as a qualitative description of the distribution of low-frequency ground motion and of which areas experience stronger shaking than others; they are not a quantitative estimate of what the peak ground motion may be. Additional quantitative modeling of broadband ground motions for northern SJF ruptures can be found in the companion paper to this study (Lozos, Olsen, *et al.*, 2015).

Fault Geometry

Our model encompasses the area from the northwestern end of the SJF in Cajon Pass to the known seismic gap in Anza, for a model fault length of 106.8 km. We take our fault geometry from the USGS Quaternary Fault Database (see Data and Resources). In this parameterization, the Claremont strand is 75.6 km long, the Casa Loma–Clark strand is 55 km long, and the Farm Road strand is 2.4 km long. All three strands have a basal depth of 16 km. The USGS Quaternary Fault Database (see Data and Resources) consists of surface traces only; however, many of the smaller bends and discontinuities in the surface trace may smooth out into a more planar surface at depth. As there is no high-resolution data for the geometry of the SJF below the surface, we choose to use the surface trace geometry at depth. Extension of the complex surface geometry to depth results in a highly heterogeneous pattern of stresses (discussed below) for the whole seismogenic thickness of the fault, which may induce more barriers and potential endpoints than a smoother fault would. Thus, we consider this geometry to be an end-member case

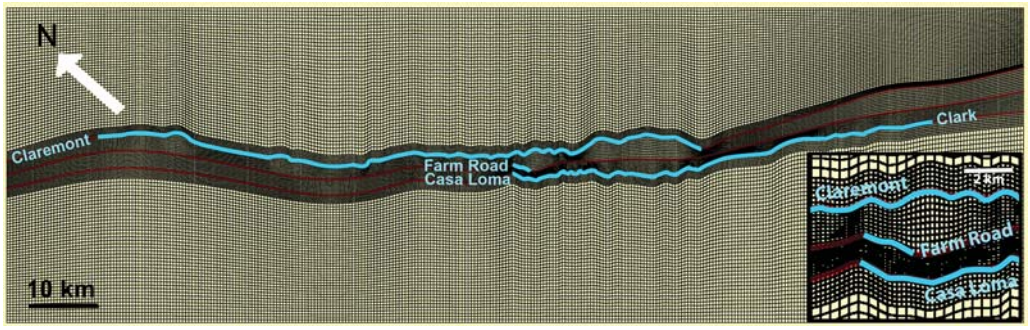

Figure 3. FaultMod mesh of the northern SJF, with a model geometry based on the USGS Quaternary Faults Database (see Data and Resources). The Claremont strand is the topmost strand in this figure. The parts of the fault system that are permitted to rupture are marked in blue. A close-up of the northwestern end of the stepover region is inset in the lower right corner. The larger elements on the outside of the figure are 400 m^2, and the smaller ones surrounding the fault are 200 m^2.

for extreme geometrical complexity, opposite from the planar approximations used in many modeling studies of real-world faults. Other smoother interpretations of the geometry of the northern SJF exist (e.g., Marliyani *et al.*, 2013; Onderdonk *et al.*, 2015; Rockwell *et al.*, 2015), but we choose to use the complex end member in this study because we believe it provides the clearest illustration of how different scales of geometrical complexity may affect the rupture process.

We assign all three fault strands a vertical dip. This is how the SJF is represented in the SCEC Community Fault Model (Plesch *et al.*, 2007), which is corroborated by seismicity (Lin *et al.*, 2007) and geology (Kendrick and Morton, 2012). Incorporating variation in dip would lead to further heterogeneity in the stress state of the fault; however, because complexity down dip is not as well understood as the complexity of the surface trace, we elected to focus on along-strike complexity and keep the down-dip geometry more simplified.

Our fault mesh is generated within FaultMod and is shown in Figure 3. The complex geometry is constructed based on a series of latitude–longitude waypoints with spline curves extrapolated between them. This method is capable of capturing geometrical complexity on a smaller scale than the grid size; our smallest scale geometrical complexity is comparable to our 200 m element size.

Velocity Structure

Our models incorporate the SCEC Community Velocity Model (CVM-S, v. 4; Magistrale *et al.*, 2000; Kohler *et al.*, 2003), rather than embedding the faults in a homogeneous or simplified material setting. However, the element size required for our models to be computationally feasible is large enough that we would not be able to resolve high-frequency ground motions produced in the lowest-velocity regions of the model. To ensure that we are resolving ground motions up to 1 Hz, we clip the minimum *P*- and *S*-wave velocities to the values listed in Table 1. This results in a smoothing of some of the details of the velocity structure, particularly in the case of boundaries between sedimentary rock and unconsolidated sediment. The effects of the clipping are most pronounced in regions of deep low-velocity material, such as the San Bernardino basin; velocities at most hard rock sites are above the cutoff and are therefore not clipped. A hybrid modeling procedure can be used to resolve ground motions from the full range of velocities in the CVM-S (see Lozos, Olsen, *et al.*, 2015).

Uniform Traction Models

The default way in which FaultMod assigns stresses to a fault is to apply specified shear and normal stress values everywhere along the trace, resulting in uniform traction, dynamic stress drop, and fault strength *S*.

$$S = \frac{\sigma_y - \sigma_0}{\sigma_0 - \sigma_f},$$

in which σ_y is yield stress, σ_0 is initial shear stress, and $\sigma_0 - \sigma_f$ is dynamic stress drop, with a lower *S* value resulting in a more energetic rupture (Das and Aki, 1977). We conducted a series of uniform traction models using a uniform stress drop of 5.5 MPa, and a uniform *S* of 0.6. The forced nucleation points in these models were 8 km down dip, representing half the seismogenic thickness of the fault, at 3 km along strike from the northeast end of the Claremont strand and 3 km along strike from the southwest end of the Casa Loma strand in order to maximize directivity toward the stepover. We conducted uniform traction models with the faults embedded in a homogeneous half-space in which $V_P = 5000$ m/s, $V_S = 3100$ m/s, and $\rho = 2675$ kg/m^3 and embedded in the complex material setting of the SCEC CVM-S.

Regional Stresses

We modified FaultMod to allow it to apply a homogeneous regional stress field to the fault system, resulting in different values for shear and normal stress depending on the orientation of each part of the fault. In order to do this, we calculate the stress tensor for a chosen stress drop and fault strength *S* for a 45° northwest-striking fault, the overall orientation of the SJF. This tensor is then resolved individually onto each node of the fault.

Table 2
Model Stress States

$\sigma_{vertical}$ (MPa)	$\sigma_{north–south}$ (MPa)	$\sigma_{east–west}$ (MPa)	Stress Drop (MPa)	S (km)
20	28.5	8.5	5.5	0.5
20	29.45	9.05	5.5	0.55
20	30.05	9.5	5.5	0.6
20	53.25	17.3	9.5	0.65
25	54.9	18.3	9.5	0.7
25	56.1	19.1	9.5	0.75
20	42.2	10.2	9.5	0.25

$\sigma_{vertical}$, $\sigma_{north–south}$, and $\sigma_{east–west}$ are the vertical, north–south, and east–west principal stresses, respectively. S is the fault strength.

We use a seismicity-based regional stress field in which the maximum horizontal compressive stress is oriented N7°E (Hardebeck and Hauksson, 2001) in most of our models. We also ran several tests in which we kept the same magnitude of principal stresses as in the N7°E models but rotated their orientation 10° in either direction to test the effect of overall stress orientation on rupture extent. We conducted models with two different input dynamic stress drops, as resolved on a 45° northwest-striking planar fault: 5.5 MPa, which falls in the middle of the range of average stress drops inferred for continental strike-slip faults (Kanamori and Anderson, 1975; Kanamori and Brodsky, 2004), and 9.5 MPa, which is the inferred stress drop of the M_w 6.5 1968 Borrego Mountain earthquake, the most recent historic event on the SJF (Burdick and Mellman, 1976). Within each stress-drop case, we varied S to gauge the effect of fault strength on rupture extent. Our stress cases are described in Table 2. Although this article refers to these cases by their input stress drop and S, note that both stress drop and S become highly heterogeneous along strike as a result of the complex fault geometry.

Figure 4 depicts the regional stress field resolved as shear stress onto all three of our model fault segments. The regional normal stress field follows the same pattern, albeit with different values. Although this example is for a case with a stress drop of 5.5 MPa and an S of 0.6, the overall pattern of zones of high and low stress and strength is consistent over different values of initial S and stress drop; the only variability is in magnitude. Because the geometry is consistent between the surface and the base of the fault, the stress field produces strong horizontal variation in the stress field but no vertical variation. To compensate for decreasing confining stresses toward the surface, we taper the shear and normal stresses to 1% of their initial value over the top 3 km of the fault; this is done separately from the initial stress-field generation, which is why this effect does not appear in Figure 4. We also clip the minimum shear stress at zero to avoid the unrealistic case of the fault locally becoming left lateral.

The lettered dots in Figure 4 are points we used for the initial forced nucleation. Points A, C, D, and F are all 3 km from the end of their respective fault segments and were chosen to maximize directivity effects. Points B and E align with the end of the stepover itself; past models of extensional

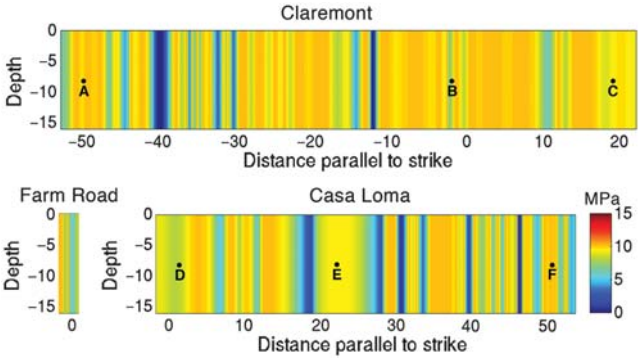

Figure 4. The shear stress distribution resulting from a regional stress orientation of N7°E resolving on the northern SJF geometry shown in Figure 3. The lettered dots indicate different locations in which we forced initial rupture nucleation. This figure was made using an input stress drop of 5.5 MPa and an input S of 0.6. Different input values produce different shear stress magnitudes, but the overall pattern of high- and low-stress areas remains the same regardless of input values.

stepovers show that, within an event, rupture jumps on to the portion of the second segment that is directly opposite the end of the first segment (Harris and Day, 1993), which means these are also plausible locations for nucleation for a second event following an initial rupture that did not jump the discontinuity.

Stochastic Stresses

To account for stress variations that may not be geometrically induced or on a regional scale, we also conducted models that combine the regional stress field described above with several different randomized stochastic stress distributions. We generate these stress fields using the method of Andrews and Barall (2011), which creates a random self-similar shear stress distribution based on a specified fault size, frictional parameters, normal stress, and four random number seeds. We used the same input frictional parameters as in the FaultMod models (listed in Table 1), and our input normal stress was the average normal stress from the regional stress field for a given S and stress drop. To insure that the smallest stochastic variability was at the scale of a single element and not inherently larger, we generated our stochastic stresses at a grid size of 60 m then stretched everything out as we combined it with the regional stress field; 60 m complexities in the stochastic stress output become 200 m complexities in the FaultMod stress-field input. The Andrews and Barall (2011) code is set up to generate a stress distribution that concentrates stochastic asperities at the center of the fault and has homogeneous stresses around the edges. Because we wanted the stochastic stresses to cover our entire faults, we generated distributions that were three times the size of our faults in terms of both strike and dip then clipped out the middle third to apply to our models. Figure 5 is an example stochastic stress distribution, with average normal stress taken from the regional stress field in Figure 4.

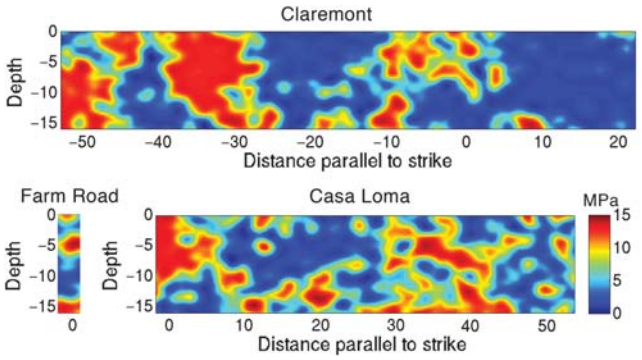

Figure 5. Example stochastic shear stress distribution. This plot was generated using an input stress drop of 5.5 MPa, an input S of 0.6, and four random number seeds. The distribution of stresses is controlled by the random number seeds and the intensity by the input stresses; for this set of random numbers, different initial stresses produce a distribution that is identical in pattern and different only in magnitude.

To combine the regional stress field with the stochastic stress distribution, first we subtracted the average shear stress of the entire regional stress field from the stochastic shear stress value for each element then added the residual shear stress for each element to the initial regional stress value at that element:

$$\tau_{\text{combined}} = [\tau_{\text{stochastic}} - \text{mean}(\tau_{\text{regional}})] + \tau_{\text{regional}}.$$

This method maintains an average shear stress value consistent with the input value for the regional stress field; if we did not subtract the regional average from the stochastic distribution, the average shear stress in the stochastic models would be systematically higher than in the regional stress or uniform traction models. Figure 6 shows four combined regional and stochastic stress realizations that we used in this study, with realization 1 corresponding to the combination of Figures 4 and 5. The lettered dots in Figure 6 represent different nucleation points. A and F correspond with the points in Figure 4 that were chosen to maximize directivity, but all of the other points were chosen to correspond with large areas of high stress, which are more realistic natural nucleation points. Table 3 describes the along-strike and down-dip locations for all of these nucleation points.

As in the models that incorporate the regional stress field alone, we taper the stresses to 1% of their initial value over the top 3 km of the fault, and we set the minimum shear stress to be zero to prevent the fault from becoming locally left lateral. In addition, we cap the maximum shear stress to be 90% of the yield stress to avoid spontaneous nucleations at localized points of high stress.

Results

Uniform Traction Models

For uniform traction models in which the fault system is embedded in a homogeneous half-space, rupture is only able to jump between the Claremont and Casa Loma strands of

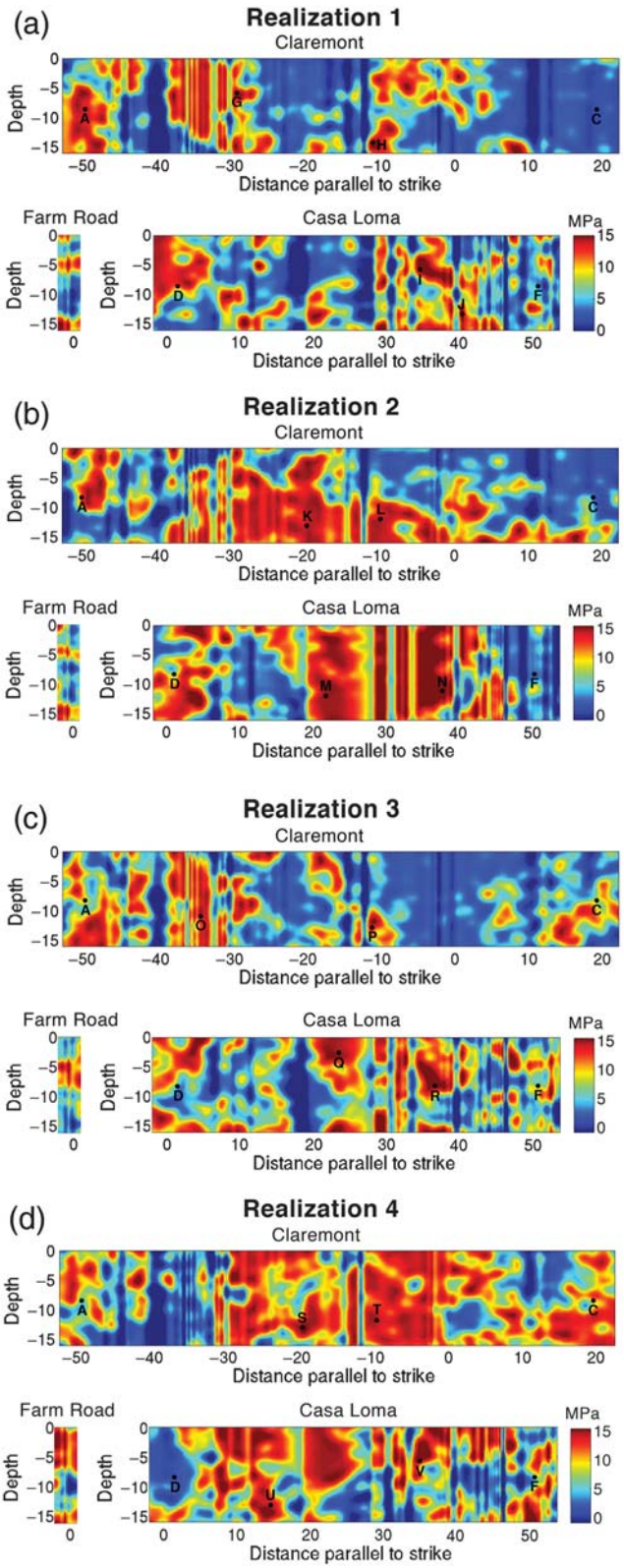

Figure 6. Full shear stress realizations, combining the regional stress field (Fig. 4) with four different stochastic shear stress distributions. The lettered dots represent different forced nucleation sites. These plots are for an input stress drop of 5.5 MPa and an input S of 0.6; different initial values do not affect the shape of the distribution, only the magnitude of the stresses.

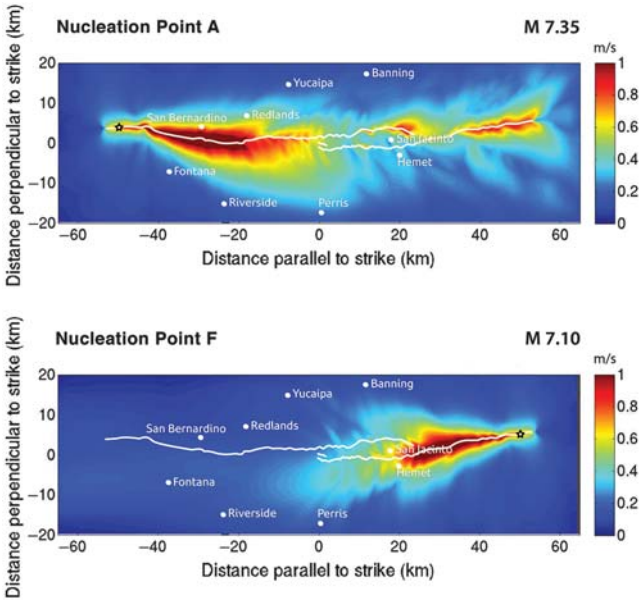

Figure 7. Peak horizontal particle velocity for ruptures on the complex SJF model geometry (white lines), with uniform traction and uniform *S*, embedded in a homogeneous material setting. The initial nucleation points are marked with stars. Even with homogeneous initial stresses and material properties, the ground-motion pattern is highly asymmetrical.

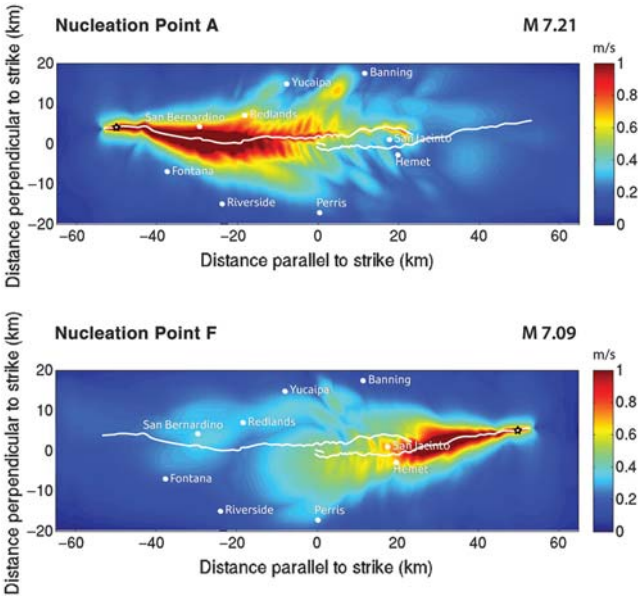

Figure 8. Peak horizontal particle velocity for ruptures on the complex SJF model geometry (white lines), with uniform traction, embedded in a heterogeneous material setting taken from the Southern California Earthquake Center Community Velocity Model-S. The initial nucleation points are marked with stars. The rupture is no longer able to jump from the Claremont strand onto the Casa Loma strand. Note that ground motions in San Jacinto, Hemet, Redlands, Banning, and Yucaipa are stronger in these models than models in which the faults are surrounded by homogeneous materials (Fig. 7).

the SJF and propagate through the whole system if rupture nucleates on the Claremont strand. The rupture does not jump if the initial forced nucleation is on the Casa Loma strand, because the complex geometry of the Casa Loma strand prevents the rupture front from even reaching the stepover region. The Farm Road strand plays no discernible role in the overall rupture behavior in either case. Figure 7 shows ground-motion plots for these models. Despite the initial uniform traction, the ground-motion distribution is highly asymmetrical about the bends in the fault, with lobes of strongest motion occurring at the end of each relatively planar section of the fault, right before the next bend. This suggests that geometry in and of itself can affect rupture behavior, even when divorced from the issue of how regional stresses resolve upon that geometry.

The uniform traction model can also illustrate the effect of the velocity structure. The models in Figure 8 use the same geometry and stresses as in Figure 7 but are placed within a heterogeneous material setting based on the SCEC CVM-S and clipped to guarantee capturing ground motions up to 1 Hz. The extent of rupture is no different for nucleation on the Casa Loma strand, but the Claremont nucleation no longer results in rupture jumping from the Claremont onto the Casa Loma. The asymmetrical ground motion around the bends in the fault remains, but the intensity and specific pattern of ground motion differ between Figures 7 and 8. Including even a clipped velocity structure in the models produces stronger ground motions in low-seismic-velocity areas such as the San Jacinto Valley (around Hemet and San Jacinto), the San Bernardino basin (around San Bernardino and Redlands), and into San Gorgonio Pass (around Banning and Yucaipa). This amplification would likely be even more pronounced if we had the computational capacity to resolve ground motions from an unclipped version of the velocity structure.

Regional Stress-Field Models

Placing the fault system within a regional stress field immediately imposes limits on the extent of rupture, as well as setting some bounds on the strength of the fault. For the 5.5 and 9.5 MPa input stress drops, we were unable to find values of *S* that both allowed rupture to jump the stepover and did not result in a spontaneous nucleation near the northern endpoint of the Claremont strand. An *S* of at least 0.6 is required to prevent spontaneous nucleation in the 5.5 MPa input stress-drop case; *S* must be 0.7 or greater in the 9.5 MPa input stress-drop case. However, these *S* values produced no ruptures that propagated through the entire length of either fault strand, let alone ones that reached or jumped the stepover. Thus, small details of fault geometry that merely caused complexity in ground-motion distribution in the uniform traction models can become either pronounced barriers or particularly favorable nucleation locations under a regional stress field. It is also worth noting that these *S* values would promote supershear rupture on a planar fault in a homogeneous setting, and perhaps on a

Table 3
Forced Nucleation Locations

Nucleation Point	Realization	Along-Strike Coordinate	Down-Dip Coordinate (km)
A	All	−50.4 km Claremont	−8
B	Regional	−1.6 km Claremont	−8
C	Regional	19.2 km Claremont	−8
D	Regional	1.4 km Casa Loma	−8
E	Regional	22.2 km Casa Loma	−8
F	All	50.4 km Casa Loma	−8
G	1	−29 km Claremont	−6
H	1	−11 km Claremont	−13
I	1	34 km Casa Loma	−6
J	1	41 km Casa Loma	−13
K	2	−20 km Claremont	−13
L	2	−10 km Claremont	−12
M	2	22 km Casa Loma	−12
N	2	37 km Casa Loma	−11
O	3	−34 km Claremont	−11
P	3	14 km Claremont	−13
Q	3	23 km Casa Loma	−3
R	3	37 km Casa Loma	−8
S	4	−20 km Claremont	−13
T	4	−10 km Claremont	−12
U	4	14 km Casa Loma	−13
V	4	35 km Casa Loma	−6

smoother interpretation of the geometry of the northern SJF, but ruptures in our models remain subshear due to the complexity of the fault geometry and stresses. Ⓔ Plots of ground motions for different input S values for the 5.5 and 9.5 MPa input stress-drop cases are shown in Figures S1 and S2, respectively, available in the electronic supplement to this article.

Using input S of 0.6 for the 5.5 MPa input stress-drop case and S of 0.7 for the 9.5 MPa stress-drop case, we conducted models with forced nucleations at the points marked in Figure 4 to determine whether the nucleation location affected the ability of rupture to jump the stepover. Figure 9 shows the results for the 5.5 MPa initial stress-drop case. None of these nucleation points produced a jump from segment to segment. A geometrical barrier toward the southern end of the Claremont strand controls the extent of all ruptures nucleating on that strand. Ruptures starting at point B, at the center of the Claremont, propagate bilaterally to Cajon Pass to the north and the persistent barrier to the south, whereas ruptures nucleating at point C, the far southern end of the Claremont, do not propagate beyond the barrier. Nucleation anywhere on the Casa Loma–Clark strand tends to produce shorter ruptures than on the Claremont; none of the nucleation points on this strand result in rupture propagation through more than 20 km of the fault. For all but one of the nucleation points on either strand, the stress drop had no effect on the extent of the rupture, the exception being point E, which produced no propagation beyond the forced nucleation in the 5.5 MPa stress-drop case and resulted in a 20 km bilateral rupture in the 9.5 MPa stress-drop case. In other models, the primary difference between the 5.5 and 9.5 MPa stress-drop cases is that the latter produce a wider distribution of stronger ground motion over the length of the rupture. Ⓔ Results for the 9.5 MPa initial stress-drop case are shown in Figure S3.

We also conducted a series of models in which we rotated the orientation maximum horizontal compressive stress 10° in either direction from N7°E, corresponding with one standard deviation away from that mean value (Hardebeck and Hauksson, 2001), while keeping the magnitudes of the principal stresses the same as in the N7°E case. In these cases, we focused on nucleation points A and E. We used the principal stress magnitudes that would correspond to the 5.5 MPa stress drop and $S = 0.6$ case and the 9.5 MPa stress drop and $S = 0.7$ case, as resolved on a 45° northwest-striking planar fault. However, changing the angle of the regional stress field changes how the stresses resolve on the fault, regardless of complexity. This results in a different effective input S and dynamic stress drop, as taken from the planar fault, and a different complex pattern of S and stress drop once the planar fault values are resolved onto the complex fault geometry. Ⓔ These models are shown in Figure S4.

Rotating the orientation of the maximum horizontal stress to N17°E resulted in shorter rupture lengths with less intense ground motions than in the N7°E case, for both nucleation locations and both stress cases. However, a maximum horizontal stress of N3°W results in ruptures that are much more energetic than in the N7°E case. For the 5.5 MPa stress-drop case, the spontaneous nucleation on the northern Claremont strand returned, and the resulting rupture propagated through the entire Claremont strand, regardless of nucleation point. In the 9.5 MPa stress case, nucleation on the Claremont and the Casa Loma alike produced jumping rupture that propagated through the entire fault system and resulted in very high ground motions.

Stochastic Stresses

We initially approached nucleation in the models with a combined regional and stochastic stress field in the same way as all the previous models: forcing nucleation at the northern end of the Claremont (point A) or the southern end of the Clark (point F) to maximize energy building up ahead of the rupture front in the direction of rupture and therefore maximizing the chances of rupture jumping from one fault strand to the other. This quickly proved not to be an effective method: even with an input stress drop of 9.5 MPa and an S value of 0.25, which would result in extremely energetic supershear rupture propagation on a homogeneous planar fault, rupture did not propagate far beyond the forced nucleation zone, as shown in Figure S5. However, the difference between the four stress realizations is enough to produce very different ground-motion distributions even in models that failed to develop self-sustaining rupture.

Given the complexity of the regional and stochastic stress realizations, we decided to approach these models

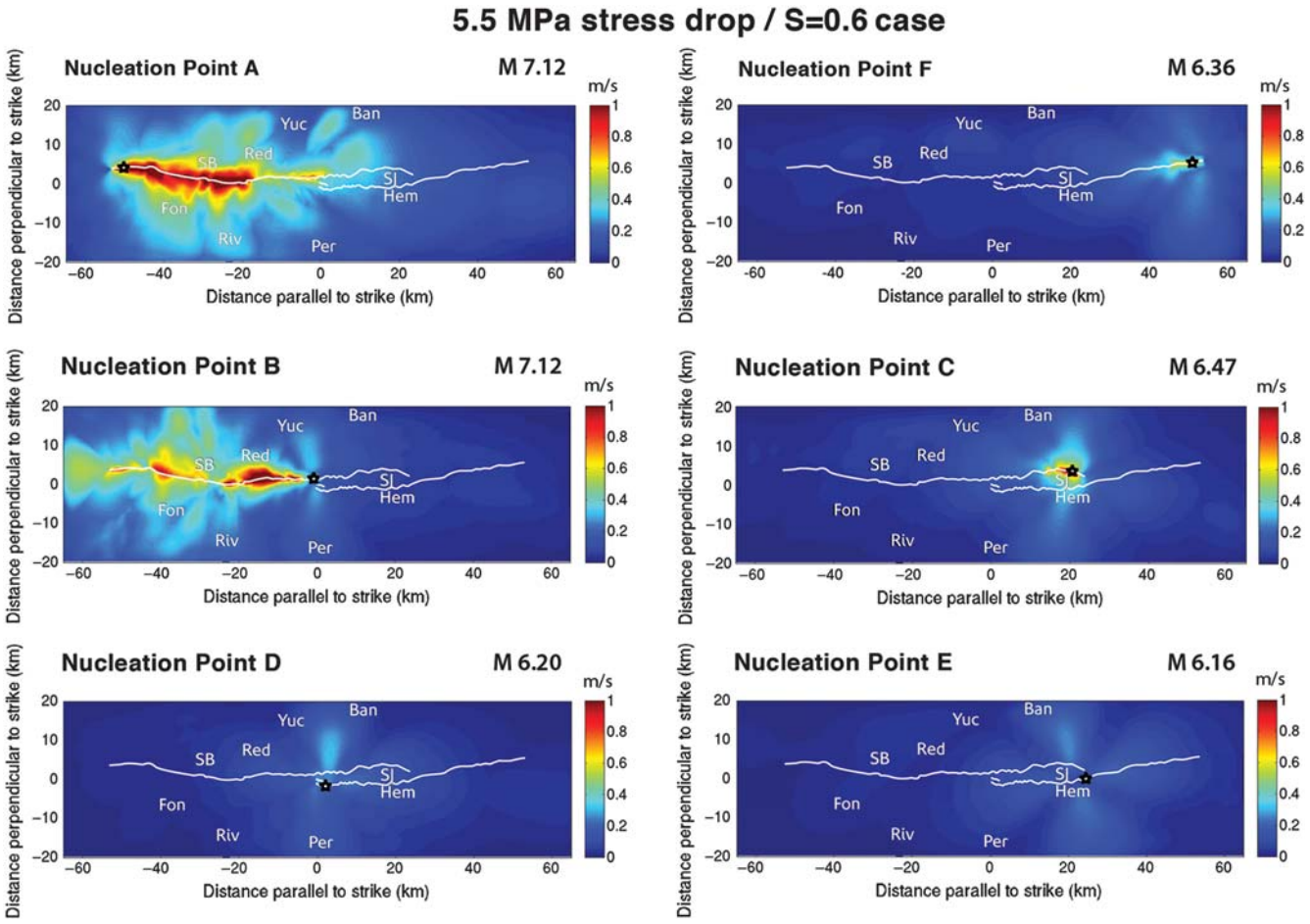

Figure 9. Peak horizontal particle velocity for ruptures on the northern SJF, with input stress drop of 5.5 MPa and input S of 0.6. Nucleation points, corresponding to Figure 4, are marked with black stars. The fault is shown in white, and the letters mark nearby cities (SB, San Bernardino; Fon, Fontana; Red, Redlands; Riv, Riverside; Yuc, Yucaipa; Per, Perris; Ban, Banning; SJ, San Jacinto; Hem, Hemet). With the exception of nucleation point B, at the center of the Claremont strand, these models result in shorter ruptures than nucleation at points A or F do.

by choosing points of particularly high shear stress within a large area of elevated shear stress as forced nucleation sites. This is a more realistic approach to nucleation, as the yield stress of a fault is most likely to be exceeded at local high points of shear stress. The resulting suite of models produced longer and more complex ruptures and allowed us to resume using the same input stress drop and S values as in the rest of this study. Figure 10 shows ground-motion distributions for 5.5 MPa stress drop and $S = 0.6$ models with different stress realizations and nucleation points. The different regional and stochastic stress realizations produce a wide range of rupture lengths and ground-motion intensities. Whether the Claremont or the Casa Loma–Clark strand sustains longer ruptures varies from realization to realization, and the persistent geometrical barrier on the Claremont from the regional stress-field models is capable of being overridden if it falls within a region of high stress from the stochastic field. Although most of these models still result in rupture that remains on the fault strand on which it nucleated, one did produce jumping rupture; that model, which used stress realization 4, had a forced nucleation on the Claremont strand. As in the models with a regional stress field only, the input stress drop for these models affected ground-motion intensity far more than it affected the extent of rupture.

Discussion

Uniform Traction Models

The asymmetrical ground-motion distribution in the uniform traction models is a result of rupture directivity and dynamic stress changes. As a rupture propagates through a relatively straight section of a fault, amplified waves ahead of the rupture front result in a buildup of energy that allows the rupture front to become more energetic. This results in increasingly strong ground motion the further rupture propagates through that straight fault section. However, as soon as rupture reaches a bend or break in the fault, directivity is broken, and the effect must build up again as rupture propagates through the next segment. Previous dynamic modeling studies on stepovers with planar segments (e.g., Lozos *et al.*,

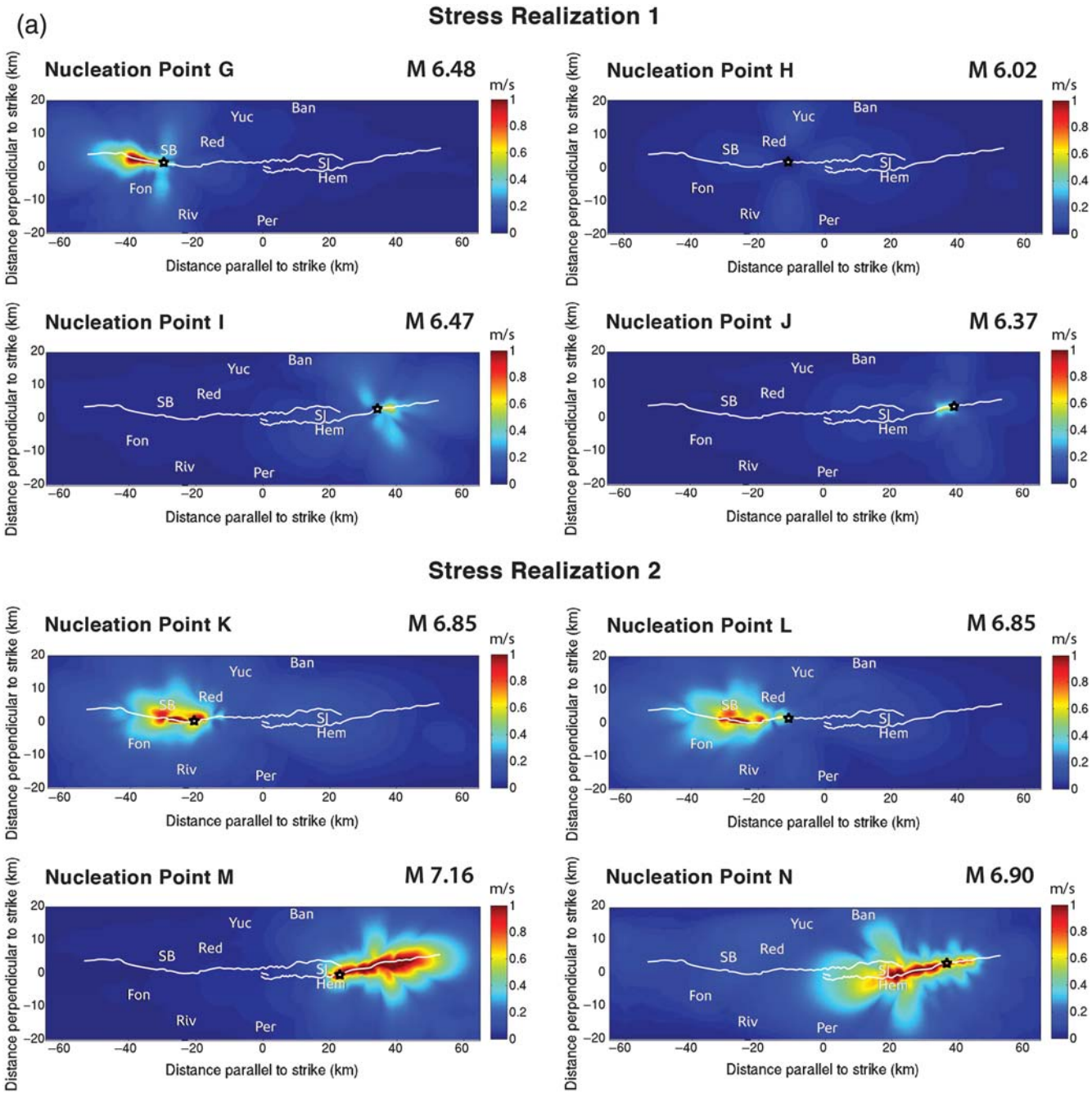

Figure 10. Plots of peak horizontal particle velocity for models incorporating four different combined regional and stochastic stress fields. The location of the initial forced nucleation in each model coincides with a local zone of high shear stress and is indicated by a black star. Each stress realization, and its associated nucleation points, is shown in Figure 6. The fault is shown in white, and the letters mark nearby cities (SB, San Bernardino; Fon, Fontana; Red, Redlands; Riv, Riverside; Yuc, Yucaipa; Per, Perris; Ban, Banning; SJ, San Jacinto; Hem, Hemet). The rupture jumps from the Claremont strand onto the Casa Loma strand when initial forced nucleation occurs at point *S*.

(*Continued*)

2013) have shown this same directivity effect. This effect explains why the weakest ground motions in the uniform traction models occur right after rupture has turned a bend in the fault trace and the strongest motions occur right before the next bend. Previous dynamic models of more simplified nonplanar faults (e.g., Oglesby and Mai, 2012) have produced similar ground-motion patterns. As such, we would expect to see similar variations in ground motion around bends in the fault trace if we were to model any other smoother interpretation of the geometry of the northern SJF.

The series of breaks in directivity that comes with rupture along a nonplanar fault also results in dynamic stress changes that may place the next section of the fault in either a region of stress increase or stress shadow, depending on its

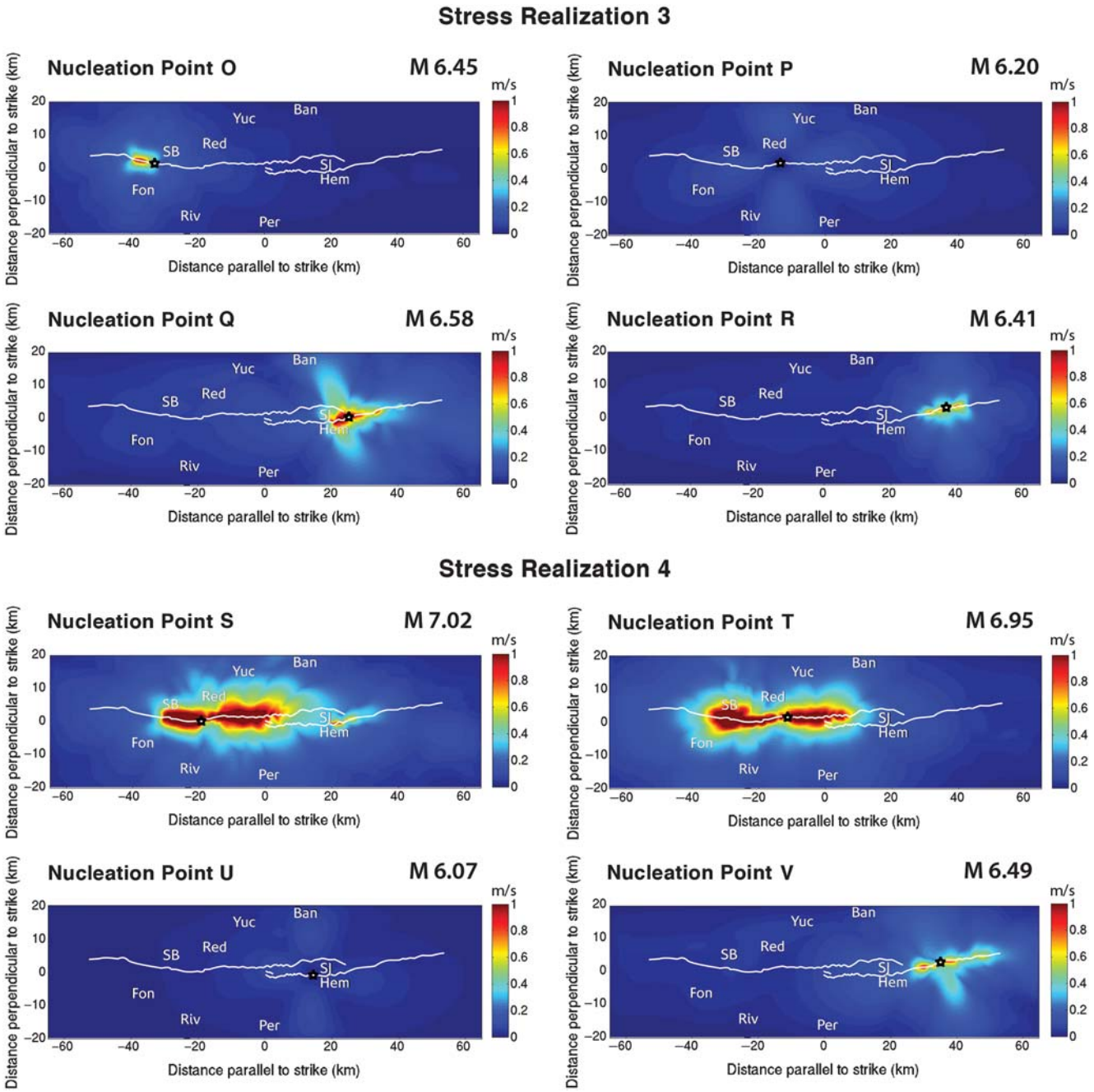

Figure 10. Continued.

orientation, thus imposing heterogeneous stresses further along strike even if the initial stress state was homogeneous. This effect makes certain parts of the fault more or less favorable for rupture than others, which is why ground-motion intensity on a given section of the fault in Figures 7 and 8 does not simply scale with the length of that segment, as it would if directivity were the only effect at work.

The fact that nonplanar fault geometry with uniform traction can still result in such heterogeneous rupture propagation and ground motion is cautionary against using a variable along-strike stress field on a planar fault as a proxy for how a regional stress field resolves on a nonplanar fault. Although the energy of the rupture front would still be very heterogeneous in such a model, there would be no break in the direction of the rupture, and therefore nothing to interrupt the buildup of waves ahead of the rupture front. Also, the area ahead of the rupture front on a planar fault is always in a region of increased dynamic stresses; the possibility of the next part of the fault falling within a region of stress shadow is lost when there is no geometrical complexity.

Our decision to include the Farm Road strand in our modeling was based on our previous modeling work, which

suggests that a small intermediate fault segment within a stepover can play a controlling role in whether rupture can jump the stepover (Lozos *et al.*, 2012; Lozos, Oglesby, *et al.*, 2015). The fact that the Farm Road strand makes no discernible contribution to the rupture process in the present study is due to both its position within the stepover and its length. In extensional stepovers, rupture jumps to a point on the second fault that is directly aligned with the end of the first segment, because that is where the lobe of increased Coulomb stress from rupture on the first fault intersects the second fault. The USGS Quaternary Faults Database (see Data and Resources) maps the 2.4-km-long Farm Road strand entirely to the interior of the Claremont–Casa Loma stepover, in a position where it would not intersect this region of stress change. If we were to model an alternate interpretation of the stepover geometry in which the Farm Road strand is 7 km long and extends beyond the northwestern end of the Casa Loma strand (e.g., Marliyani *et al.*, 2013), then the Farm Road strand would intersect the region of stress change and might be expected to sustain some coseismic slip. However, our previous work indicates that a 7-km-long intermediate fault within a stepover inhibits jumping rupture (Lozos *et al.*, 2012). Models of this alternate geometry may therefore make jumping rupture from the Casa Loma onto the Claremont even less likely than in the present study.

The inability of rupture to jump from the Claremont strand onto the Casa Loma strand in models that incorporate a complex velocity structure is a result of the rupture front losing energy as it propagates from harder rock sites into the softer sediment of the stepover region. The same effect has been described in models of planar stepovers in simplified heterogeneous velocity structures (Lozos *et al.*, 2013). The fact that it still plays a role in rupture cessation even in a more realistic model with additional levels of heterogeneity emphasizes the importance of including realistic velocity structures in models of real faults. This effect would likely produce even shorter model ruptures if we did not have to clip the velocity structure, because the contrast in properties between hard rock and soft sediment is even more pronounced.

Regional Stress-Field Models

Although we used the input stress drop and fault strength S to describe the stress cases we use in our models, the actual shear and normal stresses on the fault are modulated by the geometry, and are therefore at least as heterogeneous as the geometry itself. Figure 11 shows the actual local fault strength S over the entire fault system; though the input S is 0.6 in this case, the actual distribution of S is quite heterogeneous. As on a planar fault, the parts of the fault system with lower values of S sustain more energetic rupture, whereas higher values of S are more likely to slow or stop rupture propagation. The part of the northern Claremont strand that nucleated spontaneously at low input S corresponds with a wide zone of negative S, which results from the shear stress at the beginning of the model period already exceeding the yield

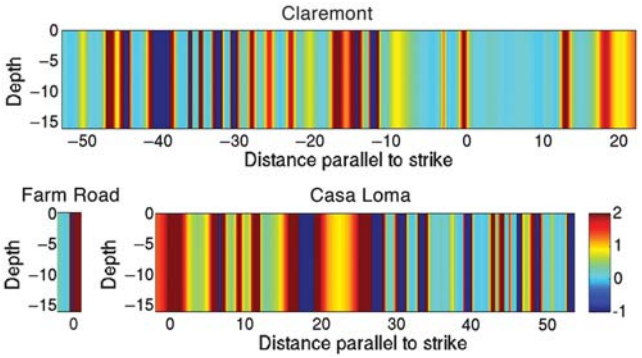

Figure 11. The fault strength parameter S for a N7°E-oriented regional stress field with an input stress drop of 5.5 MPa and an input S of 0.6. Different input values of S and stress drop would produce different effective S values but not a different pattern of relative high S to relative low S. The actual S value on most parts of the fault is not equal to the input S value. The Claremont strand has less variation in S overall than the Casa Loma strand does, and the bands of particularly high or particularly low S are wider on the Casa Loma strand than on the Claremont strand.

strength of that section of the fault. Similarly, the persistent geometrical barrier toward the southern end of the Claremont strand is a result of rupture losing energy in the high S region at −18 km along strike and being unable, in this depleted energy state, to propagate past a second high S region at 0 km along strike. Because these high and low spikes in S are so closely correlated with tight bends in the fault geometry, we expect that models of a smoother interpretation of the geometry of the SJF would not produce spontaneous nucleations nor such sharp geometrical barriers within the individual strands of the stepover system.

Areas of high fault strength pose barriers to rupture, but the size of the high S region can have more of an effect than the actual value of S on its ability to stop rupture. For a narrow high-strength patch, a rupture front may be energetic enough to simply fracture through the unfavorable area, or dynamic stress changes from rupture leading up to that point may be strong enough to renucleate on the other side of the barrier, jumping over it as if it were effectively a break in the fault trace. Directivity also affects the ability of rupture to negotiate a barrier: the more energy that has built up ahead of the rupture front, the more energy can go into fracturing through an unfavorable barrier or, failing that, the stronger the stress change that results from rupture hitting the barrier, which increases the likelihood of rupture jumping over the barrier altogether. The forced nucleation points that are closer to high S regions (e.g., the southern end of the Claremont or any of our Casa Loma–Clark nucleation points) result in shorter ruptures because the rupture front cannot build up enough directivity to negotiate the barriers.

In our models, the Claremont strand is more favorable than the Casa Loma–Clark strand for longer rupture. This is partly because the Claremont has larger areas of lower local S than the Casa Loma strand does. The Claremont has fewer geometrical complexities along its length than the Casa

Loma–Clark does, which means there are fewer places in which a bend in the trace can result in a local high-S zone. The Casa Loma–Clark has more barriers and therefore more potential rupture endpoints, as well as more limits on how much of a directivity effect a rupture can build up. Even disregarding extremely localized highs and lows in S, the Claremont strand is more favorably aligned within the regional stress field, resulting in lower S on average when compared with the Casa Loma–Clark strand. We expect that this effect alone would promote longer ruptures on the Claremont than on the Casa Loma–Clark, even in models based on a smoother interpretation of the fault geometry.

A rupture with a higher stress drop is a more energetic rupture. However, choosing a higher input stress drop versus a lower one, or a higher or lower input S, does not change the relative strength along the fault. Regardless of the actual value of S, or of shear or normal stress, barriers are still relatively high strength compared to the rest of the fault, and particularly favorable areas are still relatively low strength. This is why the higher stress-drop cases did not, for the most part, produce longer ruptures than the lower stress-drop cases. The few cases in which it did, such as in the nucleation point at the center of the Casa Loma–Clark strand, were a result of there being enough fracture energy for the rupture to propagate through narrower barriers; these ruptures still terminated at larger areas of higher S. In all of the high stress-drop models, the stronger ground motion compared to the lower stress-drop models at the same nucleation points is a result of there being more available energy budget for seismic radiation.

The results for the rotated stress-field models are directly related to the issue of relative strength and energy budget as well. Rotating the maximum horizontal compressive stress a small quantity in either direction does not significantly change the relative strength distribution across the fault; barriers and particularly favorable zones remain in the same places as in the N7°E case. However, this rotation, with the same magnitude of stresses, does change the effective input S and stress drop. The N17°E models produce shorter ruptures with weaker ground motions because the 5.5 MPa stress drop and $S = 0.6$ case becomes a 3.47 MPa stress drop and $S = 1.88$ case, and the 9.5 MPa stress drop and $S = 0.7$ case becomes 5.8 MPa stress drop and $S = 2.23$. The overall fault strength is higher, and there is less energy budget overall. Conversely, the N3°W models produce jumping rupture with extreme ground motions because the 5.5 MPa stress drop and $S = 0.6$ case becomes a 6.5 MPa stress drop and $S = 0.11$ case and the 9.5 MPa stress drop and $S = 0.7$ case becomes 11.26 MPa stress drop and $S = 0.23$. The entire fault system is more favorable for rupture under these conditions, and the rupture fronts are energetic enough to fracture through or jump over most of the higher-strength barriers.

This interpretation initially may appear to contradict our result that the choice of input S and stress drop does not have a large effect on rupture extent. However, past work on the correlation between dynamic weakening and initial stresses suggests that doubling the initial stresses and halving the critical weakening distance are equivalent and vice versa (Lozos *et al.*, 2014). Thus, a high input stress drop effectively reduces the critical weakening distance of the fault, regardless of the model input critical weakening distance. This coupled with a very low fault strength results in an energetic rupture front that does not need to rebudget much energy into fracture when it encounters a high-strength barrier. Similarly, a low input stress drop and a high input S leads to an effectively larger critical weakening distance, a less energetic rupture front, and more energy expended on fracture than on seismic radiation. These effects are not readily apparent in the N7°E models because our input S values for both input stress-drop cases are close to one another. The extremely high and extremely low input S values that occur as a result of rotating the stress field allow this effect to have more of a controlling role in the extent of the rupture.

Stochastic Stress Models

The models in which we combine stochastic stress field with the regional stress field result in more complex rupture behaviors and ground-motion distributions, because the down-dip homogeneity of stresses in the models with only a regional stress field is broken, in addition to the along-strike heterogeneity being made more complicated. Rupture behavior in these models is still controlled by the distribution of low strength and high favorability areas and the ability of a rupture to build up enough energy to fracture through or jump over a high-strength barrier. However, the irregular shape and distribution of these barriers and asperities, coupled with the geometrical complexity of the fault trace, makes it considerably more difficult for a consistent directivity effect to develop, and also greatly complicates the pattern of dynamic stress transfer that occurs when rupture reaches a bend or barrier.

In general, the relatively high-strength areas of the fault are larger in the combined regional and stochastic stress-field models, and they tend to surround the high shear stress and low-strength asperities. This is a sharp contrast to the regional stress-field models, in which the high-strength barriers are narrow features that are surrounded by lower stress regions. This results in the extents of ruptures being confined by the extent of the high shear stress and low-strength stress patches in which they nucleate. The reason our arbitrary forced nucleation points at the end of either fault segment did not produce extensive rupture (Ⓔ Fig. S5) is that in all four stress realizations, that point did not lie in or near a large region of high stress. Forced nucleation in a low shear stress and high-strength area did not result in a self-sustaining rupture at all, whereas forced nucleation in a smaller area of high shear stress and low strength resulted in rupture that died upon reaching the ends of the patch. These results are corroborated by inversions of real earthquakes conducted by Mai *et al.* (2005), which suggest that nucleation tends to

occur within or near a zone of high slip and therefore also high stress or low strength. Because the shape of the stochastic stress asperities is the biggest control of rupture extent in this set of models, we expect that models using a smoother SJF geometry would not have significantly different rupture extents from our present rough geometry models.

As in the regional stress-field models, rupture is able to propagate through or around a localized high-strength area if the rupture front is energetic enough or the high-strength patch is small enough. The stochastic distributions also bring up the question of rupture's ability to propagate through a narrow zone of low fault strength surrounded by larger areas that are not favorable for rupture. We find that, the narrower the low-strength area, or the longer the distance it spans between larger asperities, the more likely it is to arrest rupture before it can reach the next large asperity. Thus, stress distributions with more large asperities that are more closely connected (realizations 2 and 4) are able to sustain longer ruptures than realizations where the asperities are smaller and more widely distributed (realizations 1 and 3). Furthermore, in order for rupture to jump the stepover, both the end of the first fault segment and the area aligned with that endpoint on the next segment must be high shear stress and low-strength areas.

Ground-motion distributions in the stochastic and regional stress realization models are also more variable and irregular than in the models incorporating only a regional stress field. This is explainable by the interaction between directivity and geometrical spreading. Ground motion is strongest in the direction of rupture propagation, both along strike and up-dip. The strongest shaking would result from nucleation at the lower edge of an asperity, because that allows for the most directivity to develop in both spatial dimensions. However, if that asperity were to be located near the base of the fault, much of the energy would attenuate and spread before reaching the surface, resulting in weaker intensities at the surface than if the asperity were closer to the top of the fault.

Conclusions

There are many types of complexity in real fault zones, and all of these factors contribute to rupture behavior and ground-motion intensity and distribution. Complicated fault geometry alone leads to a complex interaction of directivity and dynamic stress transfer effects. A regional stress field resolved onto that geometry produces a static prerupture stress distribution that is highly heterogeneous along strike. Incorporating random distributions of high shear stress asperities, as are inferred to exist on real faults by way of inversions of real earthquakes, makes the distribution of high- and low-strength areas on the fault even more heterogeneous. When all of these effects are combined into a single model, the effect of any one factor is less evident in the results when compared with a model that isolates that factor, but leaving out any of these details produces very different results from models that include it. We therefore suggest that it is crucial to include as many levels of realistic complexity as is computationally feasible when one is constructing models to investigate the behavior of a specific real-world fault.

The distribution of stresses on the fault, and how strong or weak different parts of the fault are relative to each other, are the controlling factor in rupture behavior, regardless of which levels of model complexity are used in producing that stress state. Sustained rupture propagation is promoted within large areas of high shear stress or low fault strength and in areas with fewer breaks in directivity. Rupture is able to propagate through a higher strength area if it is energetic enough to fracture through that area while still retaining enough energy for propagation and radiation of seismic energy or if the stress changes induced by rupture stopping at the high-strength area are strong enough to cause rupture to renucleate on the other side of the barrier (much like what determines whether or not rupture can jump across a stepover in the fault trace). For a given input fault strength, a higher stress drop results primarily in stronger ground motion, because there is more energy budget for seismic radiation, though it may result in rupture propagation through some smaller barriers. For a given input stress drop, lower values of input fault strength produce longer ruptures.

Pertaining to the northern SJF specifically, we find that the Claremont strand is more favorable for longer ruptures than the Casa Loma–Clark strand. This is due in part to the fact that a maximum horizontal compressive stress orientation of N7°E produces lower S values on the Claremont than on the Casa Loma–Clark and also because the Claremont has less geometrical complexity, and therefore fewer potential barriers, along its trace than the Casa Loma–Clark does. With or without a stochastic stress distribution combined with the regional stress field, very few of our models produce jumping rupture from the Claremont onto the Casa Loma or vice versa, and even fewer produce an end-to-end rupture on either strand of the fault. The tendency of our models to produce shorter ruptures, even when nucleation is forced at the most favorable points within the largest asperities, is consistent with the SJF's historical behavior. We cannot say whether the barriers that stopped rupture in historic northern SJF events are purely geometrical or are a result of other features of the stress distribution on the fault, because we do not know the real-world distribution and shape of its nongeometrical asperities. More detailed analysis of seismicity would be useful both for determining the geometry of asperities and of the fault itself at depth and could lead to production of even more realistic models of the SJF.

The historical and model tendency for the SJF to produce shorter ruptures is a good thing from a hazard standpoint, because fewer communities would be severely affected by such a rupture than one that propagated through an entire segment or across the stepover. However, neither our models nor paleoseismology can rule out the possibility of jumping rupture altogether. Furthermore, all of the longest ruptures our models produce involve the northern part of the

Claremont strand, which runs through the most densely populated parts of the Inland Empire and is surrounded by the soft sediments of the San Bernardino basin. Thus, even with its tendency to produce short ruptures, the northern SJF still poses a significant hazard to its surrounding region. Our continued work on the northern SJF (see Lozos, Olsen, *et al.*, 2015) involves higher resolution models that are able to encompass the full frequency range of ground motions that would result from a number of scenario ruptures. These models serve the dual purpose of describing shaking hazard from possible future events, and of comparison with the locations of precariously balanced rocks near the fault trace to help constrain possible extents of historic events.

Data and Resources

Our initial model conditions were drawn from several existing bodies of work. Our fault geometry was based on the U.S. Geological Survey (USGS) and California Geological Survey Quaternary Faults Database (http://earthquake.usgs.gov/hazards/qfaults/; last accessed October 2014), and we used the Southern California Earthquake Center Community Velocity Model-S for our velocity structure (Magistrale *et al.*, 2000). We generated complex initial stresses using the method of Andrews and Barall (2011). All of our model results were generated using FaultMod (Barall, 2009). A modified version of Figure 1 also appears in the companion study by many of the same authors (Lozos, Olsen, *et al.*, 2015). All other figures were generated specifically for this article.

Acknowledgments

We would like to thank Michael Barall for his help and support in modifying FaultMod to perform this type of complex modeling. We would also like to thank Philip Maechling for help with implementing the Southern California Earthquake Center Community Velocity Model, and Jacqueline Gilchrist for help with implementing complex initial stresses. We also gratefully acknowledge Gareth Funning and James Dieterich for helpful discussion on this work, and we thank two anonymous peer reviewers for their helpful commentary and critique. Funding for this research was provided by U.S. Geological Survey National Earthquake Hazards Reduction Program Grant Numbers G12AP20064 and G12AP2006.

References

Andrews, D. J. (1976). Rupture propagation with finite stress in antiplane strain, *J. Geophys. Res.* **81,** 3575–3582.

Andrews, D. J., and M. Barall (2011). Specifying initial stress for dynamic heterogeneous earthquake source models, *Bull. Seismol. Soc. Am.* **101,** 2408–2417.

Aochi, H., E. Fukuyama, and M. Matsu'ura (2000). Spontaneous rupture propagation on a non-planar fault in 3-D elastic medium, *Pure Appl. Geophys.* **157,** 2003–2027.

Barall, M. (2009). A grid-doubling technique for calculating dynamic three-dimensional spontaneous rupture on an earthquake fault, *Geophys. J. Int.* **178,** 845–859.

Burdick, L. J., and G. R. Mellman (1976). Inversion of the body waves from the Borrego Mountain earthquake to the source mechanism, *Bull. Seismol. Soc. Am.* **66,** 1485–1499.

Das, S., and K. Aki (1977). A numerical study of two-dimensional spontaneous rupture propagation, *Geophys. J. Roy. Astron. Soc.* **50,** 643–668.

Duan, B., and D. D. Oglesby (2007). Nonuniform prestress from prior earthquakes and the effect on dynamics on branched fault systems, *J. Geophys. Res.* **112,** no. B05308, doi: 10.1029/2006JB004443.

Hardebeck, J. L., and E. Hauksson (2001). Crustal stress field in southern California and its implications for fault mechanics, *J. Geophys. Res.* **106,** 21,859–21,882.

Harris, R. A., and S. M. Day (1993). Dynamics of fault interaction: Parallel strike-slip faults, *J. Geophys. Res.* **98,** 4461–4472.

Harris, R. A., R. J. Archuleta, and S. M. Day (1991). Fault steps and the dynamic rupture process—2-D numerical simulations of a spontaneously propagating shear fracture, *Geophys. Res. Lett.* **18,** 893–896.

Harris, R. A., M. Barall, R. Archuleta, E. Dunham, B. Aagaard, J. P. Ampuero, H. Bhat, V. Cruz-Atienza, L. Dalguer, P. Dawson, *et al.* (2009). The SCEC/USGS Dynamic Earthquake Rupture Code Validation Exercise, *Seismol. Res. Lett.* **80,** 119–126, doi: 10.1785/gssrl.80.1.119.

Ida, Y. (1972). Cohesive force across the tip of a longitudinal shear crack and Griffith's specific surface energy, *J. Geophys. Res.* **77,** 3796–3805.

Kame, N., J. R. Rice, and R. Dmowska (2003). Effects of pre-stress state and rupture velocity on dynamic fault branching, *J. Geophys. Res.* **108,** 2265, doi: 10.1029/2002JB002189.

Kanamori, H., and D. L. Anderson (1975). Theoretical basis of some empirical relations in seismology, *Bull. Seismol. Soc. Am.* **65,** 1073–1095.

Kanamori, H., and E. E. Brodsky (2004). The physics of earthquakes, *Rep. Progr. Phys.* **67,** doi: 10.1088/0034-4885/67/8/R03.

Kendrick, K. J., and D. M. Morton (2012). Geomorphic evidence for structural evolution of the northern San Jacinto fault zone in the San Timoteo badlands, *Seismological Society of America Annual Meeting*, San Diego, California, 17–19 April 2012.

Kohler, M., H. Magistrale, and R. Clayton (2003). Mantle heterogeneities and the SCEC three-dimensional seismic velocity model version 3, *Bull. Seismol. Soc. Am.* **93,** 757–774.

Lin, G., P. M. Shearer, and E. Hauksson (2007). Applying a three-dimensional velocity model, waveform cross correlation, and cluster analysis to locate southern California seismicity from 1981 to 2005, *J. Geophys. Res.* **112,** doi: 10.1029/2007JB004986.

Lozos, J. C., J. H. Dieterich, and D. D. Oglesby (2014). The effects of d_0 on rupture propagation on fault stepovers, *Bull. Seismol. Soc. Am.* **104,** doi: 10.1785/0120130305.

Lozos, J. C., D. D. Oglesby, and J. N. Brune (2013). The effects of fault stepovers on ground motion, *Bull. Seismol. Soc. Am.* **103,** 1922–1934.

Lozos, J. C., D. D. Oglesby, J. N. Brune, and K. B. Olsen (2012). Small intermediate fault segments can either aid or hinder rupture propagation at stepovers, *Geophys. Res. Lett.* **39,** doi: 10.1029/2012GL053005.

Lozos, J. C., D. D. Oglesby, J. N. Brune, and K. B. Olsen (2015). Rupture propagation and ground motion on strike-slip stepovers with intermediate fault segments, *Bull. Seismol. Soc. Am.* **105,** doi: 10.1785/0120140114.

Lozos, J. C., D. D. Oglesby, B. Duan, and S. G. Wesnousky (2011). The effects of fault bends on rupture propagation: A geometrical parameter study, *Bull. Seismol. Soc. Am.* **101,** 385–398.

Lozos, J. C., K. B. Olsen, J. N. Brune, R. Takedatsu, R. Brune, and D. D. Oglesby (2015). Broadband ground motions from dynamic models of rupture on the northern San Jacinto fault, and comparison with precariously balanced rocks, *Bull. Seismol. Soc. Am.* **105,** no. 4, doi: 10.1785/0120140328.

Magistrale, H., and S. M. Day (1999). 3D simulations of multi-segment thrust fault rupture, *Geophys. Res. Lett.* **26,** 2093–2096.

Magistrale, H., S. Day, R. Clayton, and R. Graves (2000). The SCEC southern California reference three-dimensional seismic velocity model version 2, *Bull. Seismol. Soc. Am.* **90,** no. 6B, S65–S76.

Mai, P. M., P. Spudich, and J. Boatwright (2005). Hypocenter locations in finite-source rupture models, *Bull. Seismol. Soc. Am.* **95,** 965–980.

Marliyani, G. I., T. K. Rockwell, N. W. Onderodonk, and S. F. McGill (2013). Straightening of the northern San Jacinto fault, California, as seen in the fault-structure evolution of the San Jacinto Valley stepover, *Bull. Seismol. Soc. Am.* **103,** doi: 10.1785/0120120232.

Oglesby, D. D. (2005). The dynamics of strike-slip step-overs with linking dip-slip faults, *Bull. Seismol. Soc. Am.* **95,** 1604–1622.

Oglesby, D. D. (2008). Rupture termination and jump on parallel offset faults, *Bull. Seismol. Soc. Am.* **98,** 440–447.

Oglesby, D. D., and P. M. Mai (2012). Fault geometry, rupture dynamics and ground motion from potential earthquakes on the North Anatolian fault under the Sea of Marmara, *Geophys. J. Int.* **188,** 1071–1087.

Onderdonk, N. W., S. F. McGill, and T. K. Rockwell (2015). Short-term variations in slip rate and size of pre-historic earthquakes during the past 2000 years on the northern San Jacinto Fault zone, a major plate boundary in southern California, *Lithosphere* **7,** doi: 10.1130/L393.1.

Palmer, A. C., and J. R. Rice (1973). The growth of slip surfaces in the progressive failure of overconsolidated clay, *Proc. Math. Phys. Sci.* **332,** 527–548.

Park, S. K., D. Pendergraft, W. J. Stephenson, K. M. Shedlock, and T. C. Lee (1995). Delineation of intrabasin structure in a dilational jog of the San Jacinto fault zone, southern California, *J. Geophys. Res.* **100,** 691–702.

Plesch, A., J. H. Shaw, C. Benson, W. A. Bryant, S. Carena, M. Cooke, J. Dolan, G. Fuis, E. Gath, L. Grant, *et al.* (2007). Community fault model (CFM) for southern California, *Bull. Seismol. Soc. Am.* **97,** 1793–1802.

Rockwell, T. J., T. Dawson, J. Young, and G. G. Seitz (2015). A 21-event, 4000-year history of surface ruptures in the Anza seismic gap, San Jacinto fault: Implications for long-term earthquake production on a major plate boundary fault, *Pure Appl. Geophys.* **171,** 2955–2965.

Salisbury, J. B., T. K. Rockwell, T. J. Middleton, and K. W. Hudnut (2012). LiDAR and field observations of slip distribution for the most recent surface ruptures along the central San Jacinto fault, *Bull. Seismol. Soc. Am.* **102,** 598–619.

Sanders, C., and H. Magistrale (1997). Segmentation of the northern San Jacinto fault zone, southern California, *J. Geophys. Res.* **102,** 27,453–27,467.

Wesnousky, S. G. (1986). Earthquakes, quaternary faults, and seismic hazard in California, *J. Geophys. Res.* **91,** 12,587–12,632.

Working Group on California Earthquake Probabilities (WGCEP) (1995). Seismic hazard in southern California: Probable earthquakes, 1994 to 2024, *Bull. Seismol. Soc. Am.* **85,** 379–439.

Department of Earth Sciences
University of California
Riverside, California 92521
jlozos@stanford.edu
david.oglesby@ucr.edu
(J.C.L., D.D.O.)

Department of Geological Sciences
University of Nevada, Reno
1664 N. Virginia Street
Reno, Nevada 89557-0172
brune@seismo.unr.edu
(J.N.B.)

Department of Geological Sciences
MC-1020
5500 Campanile Drive
San Diego State University
San Diego, California 92182-1020
kbolsen@mail.sdsu.edu
(K.B.O.)

Manuscript received 31 October 2014;
Published Online 28 July 2015